Wideband Backscattering From Alpine Snow Cover: A Full-Season Study

Reza Naderpour, Mike Schwank, Derek Houtz, Charles Werner, *Life Senior Member, IEEE*, and Christian Mätzler

***Abstract*— This article experimentally investigates relationships between copol backscattering at a wide range of frequencies (L- to Ka-bands) and snow–ground state parameters (SPs) in different evolution phases during the full winter cycle of 2019/2020. Backscattering coefficients from 1 to 40 GHz, *in situ* snow–ground SPs, and meteorological data are measured at the Davos-Laret Remote Sensing Field Laboratory (Switzerland). Relative strengths of the snow–ground system's three primary scattering elements (air–snow interface, snow volume, and snow–ground interface) on backscattering are assessed. An anticorrelation between reasonably high snow wetness and backscattering coefficient is found, especially at higher microwave frequencies. For small amounts of snow wetness, backscatter coefficients at L- and S-bands are intensified via increasing snow volume and snow surface scattering. Snow–ground SPs influence backscattering according to their characteristic time scales of temporal evolution. Under dry snow conditions and at low and intermediate frequencies, ground permittivity is the major influencer of backscatter at a time scale of roughly two weeks. Snowfall is the major influencer of backscatter at a time scale of a few hours to a few days. The findings of this article are valuable to the development of retrieval algorithms using machine learning while maintaining a grasp on the ongoing physical processes. Another key message is that multifrequency active microwave measurements are critical to maximize the number of retrievable SPs and their estimation accuracy. For example, while Ka-band performs well in the detection of snow cover, L-band measurements are more responsive to changes of snow water equivalent (SWE) under moist or wet snow conditions.**

***Index Terms*— Alpine snow cover, backscattering, microwave remote sensing, snow water equivalent (SWE).**

I. Introduction

SNOW is a form of water that plays essential roles on earth, ranging from the water cycle and climate system to ecology, agriculture, freshwater storage, hydropower production, natural hazards, and greenhouse gas release in northern latitudes. Passive and active microwave remote sensing techniques have often been applied to quantify snow, a focus of various Earth observation satellite missions. For example, it was shown that microwave radiometry can be used for the estimation of snow melt and liquid water content [1]–[7], snow density [3], [8]–[10], and subnivean soil freeze/thaw [8], [11]–[14]. Numerous studies also applied active microwave remote sensing to the goal of estimating snow properties. Examples include estimation of snow cover extent [15]–[17], snow wetness [18], and snow water equivalent (SWE) [19]–[22].

According to various radiative transfer models, such as the Microwave Emission Model of Layered Snowpacks 3 [23], [24] and active (MEMLS 3&a) [25], and dense media radiative transfer (DMRT) models (see [26] and references therein), the frequency-dependent backscattering coefficient changes with variations in the snow and the subnivean layer's state parameters (SPs), such as snow wetness, microstructure, density, height, and, consequently, SWE and ground permittivity. Backscatter's sensitivity to these SPs has been partially validated based on experimental data [25], [26] and is a motivation for the efforts to retrieve SWE from active measurements. SWE has previously been retrieved from active microwave measurements only with season and location-specific successes over a limited range of frequencies. For example, synthetic aperture radar interferometry (InSAR) has been used for the estimation of temporal SWE changes using C-band (5.4 GHz) [20], X-band (10 GHz), and Ku-band (16 GHz) measurements [27]. L-band (1–2 GHz) radar has been used to retrieve snow density and subnivean layer permittivity [28]. Other attempts are made to estimate snow depth using the backscatter coefficient measured at C- to Ku-bands [29]–[31]. While such studies are highly valuable and informative, they face some major challenges. First, methods for estimating snow properties are usually developed for use with available satellite data at specific frequencies and acquisition schemes. This limits the research potential, which can be fully realized with multifrequency and even active–passive measurements. Examples such as the Snow and Cold Land Processes (SCLP) satellite [32] recommended to the National Aeronautics and Space Administration (NASA) in 2007, the Nordic Snow Radar Experiment (NoSREx) campaign between 2009 to 2013 [33], [34] in support of phase-A studies of the proposed mission Cold Regions Hydrology High-Resolution Observatory for SCLP (CoReH2O) [35], and NASA's Soil Moisture Active Passive (SMAP) satellite [36], [37] are clear signs of the snow remote sensing community's lasting interest in the synergistic use of active- and passive microwave remote sensing in application to snow. Second, the majority of retrieval methods partially or entirely rely on a significant number of *in situ* measurements for tuning

Manuscript received July 9, 2021; revised September 10, 2021; accepted September 10, 2021. Date of publication October 5, 2021; date of current version January 21, 2022. This work was supported in part by the European Space Agency through the SnowLab-NG Project under Grant 4000130865/20/NL/FF/AN and in part by the Swiss National Science Foundation through the APRESS Project under Grant 200020_182049. *(Corresponding author: Reza Naderpour.)*

Reza Naderpour and Derek Houtz are with the Swiss Federal Institute for Forest, Snow, and Landscape Research, CH-8903 Birmensdorf, Switzerland (e-mail: reza.naderpour@wsl.ch).

Mike Schwank is with the Swiss Federal Institute for Forest, Snow, and Landscape Research, CH-8903 Birmensdorf, Switzerland, and also with GAMMA Remote Sensing AG, CH-3073 Gümligen, Switzerland.

Charles Werner and Christian Mätzler are with GAMMA Remote Sensing AG, CH-3073 Gümligen, Switzerland.

Digital Object Identifier 10.1109/TGRS.2021.3112772

empirical models to the microwave measurements. While *in situ* measurements are important for validating remote sensing retrievals, they should ideally not be used arbitrarily to account for poorly understood relationships between backscatter and an evolving snowpack.

In this article, we experimentally investigate relationships between snow and ground SPs and backscattering coefficient at a wide range of frequencies (L- to Ka-bands) and in different snowpack evolution phases. Similar to [38]–[42], this study is focused on the experimental investigation of the possibilities and limits of active and passive microwave remote sensing for estimation of snow and subsurface properties. The key novelties of this work are: 1) wideband (1–40 GHz) phase-coherent polarimetric scatterometer data; 2) measurements of the full season snowpack evolution (before onset to after meltdown) together with comprehensive *in situ* measurements; and 3) the synergistic use of passive and active microwave remote sensing for the presented research.

We determine the primary scattering elements of the snow–ground system along with their time scale and relative strength under different snowpack conditions through the winter season. Investigation and quantification of such relationships are keys to developing a snow property retrieval algorithm, which considers the physics of microwave radiative transfer through the snow at a reasonable level of complexity. This knowledge can reduce the effect of empirical model parameter fine-tuning on the retrieval results; therefore, it will result in methods that are independent of specific times and/or regions.

In the following, we first describe the research site hosting tower-based radiometry and scatterometry, as well as *in situ* snow and meteorological measurements. Next, the used datasets are described in Section III. Analysis results on the relationship between measured backscatter coefficients and snow–ground SPs are presented in Section IV. We conclude by providing a summary of the results and the take-away messages in Section V. In this study, active measurements are conducted with the European Space Agency's (ESA) terrestrial, coherent, fully polarimetric WideBand Scatterometer (WBSCAT).

II. Research Site and Schematics

The data presented and analyzed in this article were collected at the Davos-Laret Remote Sensing Field Laboratory [43] during Winter 2019/2020. This alpine research site, situated at the Laret valley (48°50′53″ N, 6°52′19″ E) in Switzerland, is a 50 m × 50 m area at an elevation of 1450 m above sea level. The site has hosted four winter measurement campaigns since 2016. It is relatively flat with smooth topography on its southern and northwestern corners.

Fig. 1 shows site layout as implemented during the Winter 2019/2020 campaign. Tower-based L-band radiometry was conducted with the upgraded Jülich L-band radiometer—JÜLBARA [44] mounted atop a 6-m tower (RM in Fig. 1). The automatic elevation and azimuth tracking system allows for scanning different areas of the site at azimuth and elevation nadir angles $0° \leq \phi_{\text{passive}} \leq 355°$ and $30° \leq \theta_{\text{passive}} \leq 140°$,

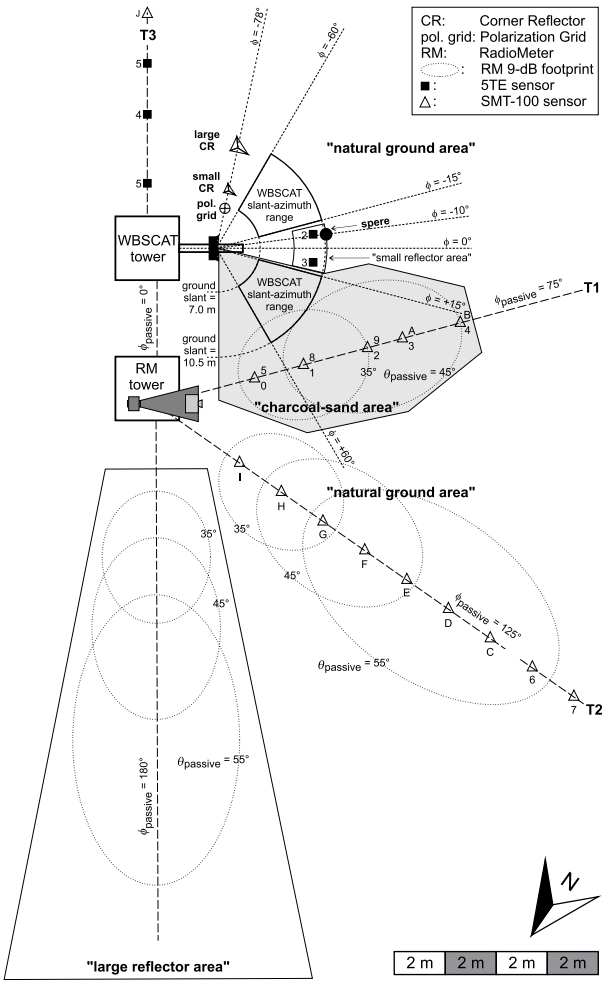

Fig. 1. Schematics of the Davos-Laret field site (48°50′53″ N, 6°52′19″ E) implemented during the winter 2019/2020 campaign.

respectively. Wideband polarimetric scatterometry was performed using ESA's WBSCAT [45]–[47], which is equipped with a precision elevation-azimuth tracking system installed approximately 6 m above ground on the "WBSCAT tower" (see Fig. 1).

In addition to the "natural ground area," two artificial footprint areas were prepared for a detailed study of the snowpack volume emission and scattering. The trapezoidal "large reflector area" allows for the measurement of the snowpack's own microwave emission, which is known to be directly related to the snow liquid water content [43], [48]. The "charcoal–sand area" was common to radiometer and scatterometer footprints, and it was prepared as an approximately 10-cm-thick layer of charcoal–soil mixture and ∼5-cm-thick layer of sand on top (see Fig. 2). The two layers, separated by a thin sheet of fleece paper, represent: 1) a smooth transition from air permittivity $\epsilon_{\text{air}} = 1$ to the permittivity $\epsilon_{\text{G}} \gg 1$ of the underlying ground and 2) a vegetation-free flat surface with nearly specular reflectivity. These features allow for investigation of scattering taking place within snowpack volume and at snow–air interface at different frequencies. The dotted ellipsoids in Fig. 1 indicate the L-band radiometer antenna's 9-dB footprint areas at different nadir angles. The "natural ground" and "charcoal–sand" footprint areas measured by WBSCAT

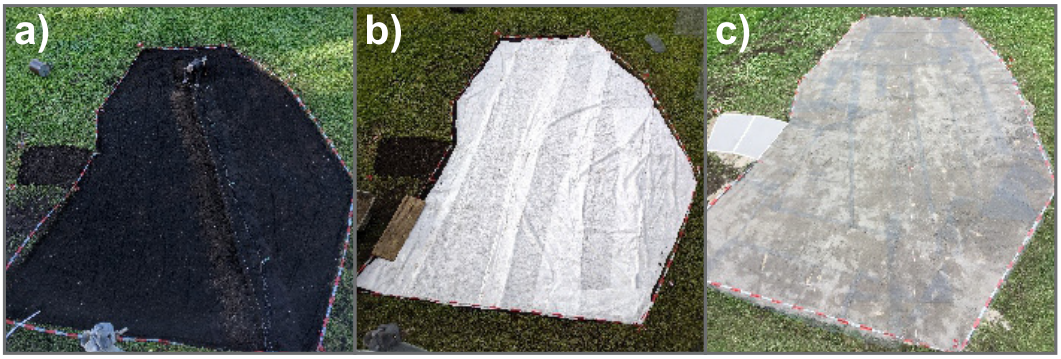

Fig. 2. Three steps for the preparation of the "charcoal–sand area." (a) Preparation of a mixture of charcoal and soil and deployment of five *in situ* sensors. (b) Placing a thin fleece to separate the two footprint layers. (c) Covering the area with fine grain sand and deployment of five additional *in situ* sensors.

correspond to the two crescents indicated in Fig. 1. They cover the ground slant range from 7 to 10.5 m. The "natural ground" and "charcoal–sand" are defined as areas encircled by the azimuth ranges $-60° \leq \phi \leq -15°$ and $+15° \leq \phi \leq +60°$, respectively. Four external WBSCAT calibration targets are marked in Fig. 1 along azimuth directions $\phi = -78°$ (trihedral corner reflectors (CRs) with square sides of 0.18 and 0.4 m, and a 0.12-m diameter polarization grid) and $\phi = -10°$ (a sphere of 0.475 m diameter). In addition, a network of 25 *in situ* soil sensors, five 5TE, and 20 SMT-100 sensors was implemented to automatically measure ground temperature T_G and relative permittivity ϵ_G. Fig. 2 shows different steps in preparing the "charcoal–sand area" and installation of *in situ* soil sensors at two different depths along the Transect 1 (T1 in Fig. 1).

III. Datasets

The nearly eight-month-long Winter 2019/2020 measurement campaign started on September 25, 2019, and was concluded on May 10, 2020. The collected data belong to three distinct categories: 1) tower-based active and passive microwave remote sensing; 2) meteorological and snow cover information; and 3) subnivean ground permittivity and temperature. Sections III-A–III-C briefly describe each category's data acquisition scheme.

A. Tower-Based Remote Sensing

Hourly L-band radiometry was performed with JÜLBARA operating at the protected frequency band (FB) of 1.400–1.427 GHz along the "charcoal–sand area," "natural ground area," and "large reflector area" at their respective azimuth angles $\phi_{\text{passive}} = 75°, 125°$, and 180°. Each elevation scan covers nadir angles $\theta_{\text{passive}} = 30°$ to $\theta_{\text{passive}} = 60°$ in 5° steps. Sky measurements, for calibration of L-band brightness temperatures, were conducted daily except for days with heavy precipitation. It was previously shown that L-band radiometry can be used for the retrieval of volumetric snow liquid water content W_S [$m^3 \cdot m^{-3}$] and snow liquid water column WC_S [mm] [3]–[5]. Given the criticality of snow wetness for emission and scattering properties of snow, L-band brightness temperatures over the "large reflector area" together with snowpack height information from the Automatic Weather Station (AWS) were used to retrieve snow liquid water column $WC_S = h_S \cdot W_S$ (assuming uniform distribution of liquid water across the snowpack profile). These data are presented in Section IV. As explained in [5], the employed L-band radiometry method for the estimation of W_S provides reliable information on the temporal variations of snowpack moisture. Considering the inverse relation between microwave penetration depth and liquid water content the quantitative accuracy of the estimated W_S is limited to the detection of snowpack wetness states: dry ($W_S \approx 0$ %), moist ($0\ \% \lesssim W_S \leq 1$ %), and wet ($W_S \gtrsim 5$ %).

TABLE I

Key Parameters in Measurement "Profiles" for Definition of WBSCAT's 2-D "Field Scans." The First to Third Numbers in Azimuth and Nadir Angle Columns Indicate the Start, Stop, and Step-Size Angles, Respectively

Band	Freq. Step [MHz]	Azimuth ϕ	Nadir Angle θ	Duration [min.]
1	2.5	$-80°, 80°, 4°$		32
2	5.0	$-75°, 75°, 3°$	$25°, 45°, 10°$	58
3	5.0	$-66°, 66°, 1.5°$		136

The baseline WBSCAT measurements were 2-D scans of the site ("field scans") to measure scattering parameters within predefined azimuth and elevation nadir angle ranges. A 2-D "field scan" is specified by a keyword-value text "profile" that specifies the operational parameters for the VNA, such as the start and stop frequencies, the number of frequency steps, receiver bandwidth, and the output signal level for calibration of the amplifiers, and backscatter power. Table I shows some of the key information in "profiles" for each of the three measurement FBs. The three angles in each row of Table I in the third and fourth columns refer to the angular span in azimuth and elevation (minimum and maximum angles) and the angular increment (last number). For a given pointing direction of the antenna boresight axis, WBSCAT data acquisition is a two-step process. First, the instrument performs an internal calibration of the VNA and RF assembly over the specified frequency range. Second, backscatter data are acquired and calibrated using the internal calibration factors and saved. For each measurement, the scatterometer performs three frequency sweeps for transmit–receive polarization combinations pp = HH, VV, and VH. A more detailed description of the procedures for internal and external calibrations of WBSCAT measurements is given in Appendix A.

Fig. 3 shows the stepwise procedure of WBSCAT data acquisition for 2-D "field scans" of the Davos-Laret Remote Sensing Field Laboratory during Winter 2019/2020 campaign. Each step is briefly described in the following.

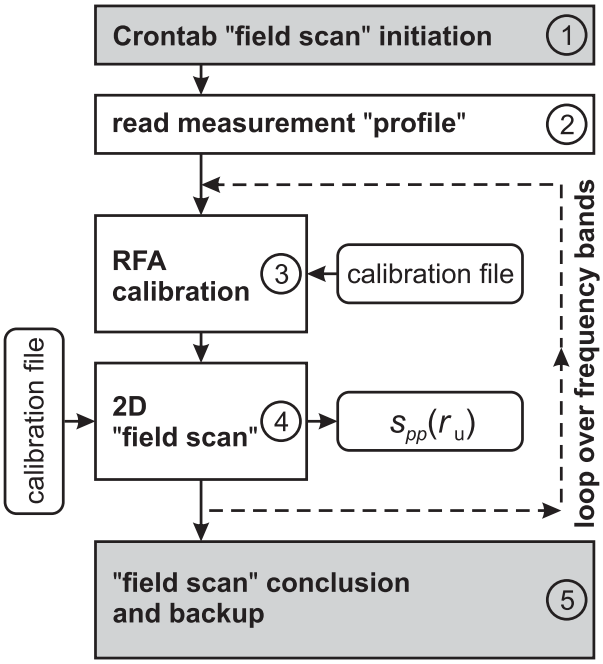

Fig. 3. Block diagram of the procedure for WBSCAT data acquisition in 2-D "field scans."

Step 1 [Crontab ("Field Scan" Initiation)]: Every day, at 3 A.M., 11 A.M., and 7 P.M., the 2-D "field scan" was initiated. This schedule ensured measurements across diurnally varying conditions of air temperature, radiation, and short-term events, such as precipitation. At the same time, it leaves enough radio-silence time for interference-free passive microwave measurements.

Step 2 (Read Measurement "Profile"): Using the contents of the "profile," the measurement scenario is defined for the instrument (see Table I).

Step 3 (RFA Calibration): Internal calibration of the radio frequency assembly (RFA) is performed for the given frequency range. The results are saved separately.

Step 4 (2-D "Field Scan"): The instrument measures backscattered signal for $pp = \text{HH}$, VV, and VH and moves in elevation θ and azimuth ϕ in predefined steps (see Table I) to cover the entire target area. The azimuth steps are selected to have at least a 50% overlap of the physical antenna aperture. Once the 2-D scan is over, Steps 3 and 4 are repeated until all FBs are covered.

Step 5 (Measurement Conclusion and Data Backup): The internally calibrated backscatter signals are backed up on external storage. The instrument is moved back to home position $(\theta, \phi) = (25°, 0°)$, and the aforementioned system components are checked to ensure their health. A log file indicates details of each scan.

B. Meteorological and Snow Data

An AWS on the site continuously measured meteorological and snow parameters, including air temperature T_{air}, precipitation (*Prec.*), snowpack height h_{S}, and SWE. This information is presented in Section IV-A. Further information regarding the AWS, measurement types, frequency, and so on is available on the research site's webpage [49].

C. Subnivean Ground Temperature and Permittivity

As mentioned in Section II, a network of 5TE [50] and SMT-100 [51] sensors along Transects 1–3 (T1, T2, and T3 indicated in Fig. 1) was used to measure temperature and permittivity (at $f \approx 100$ MHz) of the subnivean ground layers every 5 min. It is noteworthy that ground permittivity strongly depends on its water content and freeze/thaw state. The absolute value of water permittivity drops by about 40% when frequency increases from 0 Hz to 40 GHz [52]. This decrease also indicates a roughly 25% decrease in reflectivities at nadir from air to a specular surface. Ground permittivity ϵ_{G} and temperature T_{G} measurements along T2 show that the soil never froze during the campaign. The relative permittivity of the two layers in the "charcoal–sand area" is measured by five pairs of SMT-100 sensors along with T1.

IV. Results and Discussion

The purpose of this work is the investigation of relationships between snow–ground SPs and backscattering coefficient $\sigma^0_{pp}(f)$. Due to the antennas' wide field of view, differences between backscattering coefficients $\sigma^0_{\text{VV}}(f)$ and $\sigma^0_{\text{HH}}(f)$ are depressed. This results in nearly identical response of both $pp = \text{HH}$ and VV; therefore, we present only $\sigma^0_{\text{VV}}(f)$.

Our analysis of the measured backscatter signals is based on considering single-scattering mechanisms originating from three elements ($\equiv$ regimes) of the snow–ground compartment: 1) scattering from the snow–air interface; 2) volume scattering from the snowpack; and 3) scattering from the snow–ground interface. Therefore, the overarching question of this work is given as follows: what is the relative strength of each of the mentioned three scattering elements at a given frequency for different snow states? Snow wetness is also of critical importance as a primary influencer of $\sigma^0_{pp}(f)$ due to increased propagation losses with increasing snow liquid water content. This work offers the answer to this overarching question, which is presented in Table II with qualitative indicators (negligible, medium, and high) based on the presented experimental observations.

The three rows in Table II list the aforementioned scattering elements (air–snow interface, snow volume, and snow–ground interface). The six columns [cases (1)–(6)] list, in pairs, the three WBSCAT frequency ranges (1–4, 4–12, and 12–40 GHz) each under dry and wet snow conditions as estimated from passive L-band measurements over the "large reflector area" (see Fig. 1). The table must be read in columns. The relative strength of a given scattering element is indicated in each table cell. It is important to explain that this table is included already at the beginning of our results and discussion because it facilitates the explanation of our analysis results. In the following, we present detailed examples of $\sigma^0_{\text{VV}}(f)$ related to each case in Table II and provide physical reasoning behind the applied assignments.

Given the sensitivity of $\sigma^0_{\text{VV}}(f)$ to numerous ground–snow SPs, in order to study major sensitivities, we break our analysis

TABLE II

RELATIVE INFLUENCE INTENSITIES (NEGLIGIBLE, MEDIUM, AND HIGH) OF DIFFERENT SCATTERING ELEMENTS OF THE SNOW–GROUND COMPARTMENT ON THE COPOL BACKSCATTER $\sigma^0_{pp}(f)$ MEASURED FOR DIFFERENT FBS (1–4, 4–12, AND 12–40 GHz) AND DRY/WET SNOW CONDITIONS. EACH COLUMN IS GIVEN A CASE NUMBER [(1)–(6)] FOR EASY REFERRAL IN THE TEXT

	L– and S–bands		**C– and X–bands**		**Ku– to Ka–bands**	
	low frequency (1 – 4 GHz)		intermediate frequency (4 – 12 GHz)		high frequency (12 – 40 GHz)	
	dry	wet	dry	wet	dry	wet
	(1)	**(2)**	**(3)**	**(4)**	**(5)**	**(6)**
air-snow interface	negligible	medium	negligible	medium	negligible	high
snow volume	medium	high	medium	high	high	medium
snow-ground interface	high	negligible	high	negligible	medium	negligible

to first- and second-order response categories discussed in Sections IV-A and IV-B, respectively. First-order response refers to SPs of the snow–ground compartment whose effects are directly apparent from time series or scatter plots opposing their values against backscatter $\sigma^0_{VV}(f)$. Second-order responses are understood as sensitivities of $\sigma^0_{VV}(f)$ to SPs apparent only by means of time-dependent statistical analysis.

A. First-Order Response of Backscattering Coefficients

Fig. 4 shows the time series of: 1) calibrated backscattering coefficients $\sigma^0_{VV}(f)$ measured at antenna nadir angle 35° and at six frequencies representing WBSCAT's frequency range from L- to Ka-bands; 2) snow liquid water column WC_S retrieved from L-band radiometry (see Section III-A); 3)–6) SWE, snow height h_S, temperatures T_{air} and T_G, and snow precipitation *Prec.* measured by the on-site AWS (see Section III-B); and 7) ϵ_G of the sand layer in the "charcoal–sand area." Snow precipitation *Prec.* is considered as the precipitation taken place at air temperatures below freezing point $T_{air} \leq 0°C$.

To better understand the temporal variations of $\sigma^0_{VV}(f)$, we first assess the snow cover conditions during Winter 2019/2020 according to the three main SPs: h_S, WC_S, and SWE. Fig. 4(d) shows that the onset and complete melt of snow cover over the site happened on November 15, 2019, and April 17, 2020, respectively. The onset of snow cover was not a sudden clear-cut event with heavy snowfall, rather roughly one week of fluctuating increases of h_S. It is important to note the strong relative h_S fluctuations and the effect of increased snow volume scattering under dry snow conditions.

A closer look at the time series of WC_S (and h_S) indicates that the entire winter season can be broken down into seven periods (P1—P7) marked at the top of Fig. 4. This classification is beneficial to describe and understand the temporal variations of $\sigma^0_{VV}(f)$ and their relationship with SPs of the ground–snow compartment.

1) *Period 1 [Snow-Free Period (November 1, 2019–November 15, 2019)]:* Permittivity and temperature measurements indicate unfrozen moist ground during this period. Fig. 2 shows an example view of the site during this snow-free period, including a part of the "natural ground area" with low vegetation and the flat vegetation-free "charcoal–sand area."
2) *Period 2 [First Wet Snow Period (November 15, 2019–December 1, 2019)]:* A thin wet snowpack appears over the unfrozen ground. Snowpack height undergoes significant fluctuations reaching a maximum of $h_S \simeq 40$ cm and dropping down to a minimum of $h_S \simeq 15$ cm.
3) *Period 3 [First Dry Snow Period (December 1, 2019–December 17, 2019)]:* Snow accumulation continues, T_{air} decreases, and snow is dry according to WC_S derived from L-band radiometry performed over the "large reflector area."
4) *Period 4 [Second Wet Snow Period (December 17, 2019–December 5, 2020)]:* Snow accumulation continues, accompanied by $T_{air} > 0$ °C. This results in increased snow wetness demonstrated by $WC_S > 0$ mm.
5) *Period 5 [Second Dry Snow Period (January 5, 2020–February 2, 2020)]:* Snowpack enters a second dry period with $h_S \approx 70$ cm. Near the end of P5, a strong dry snow precipitation event increases snowpack height to ∼100 cm.
6) *Period 6 [Early Spring Period (February 2, 2020–March 8, 2020)]:* T_{air} follows a nearly weekly fluctuation pattern where temperature reaches a maximum of ∼ 10 °C and drops to a minimum of ∼ −14 °C. As a result, snow liquid water-column fluctuates while never dropping to $WC_S = 0$ mm. It is noteworthy that snow accumulation continues resulting in steadily increasing SWE and an increasing trend in h_S, including significant fluctuations.
7) *Period 7 [Snow Melt and Run-Off (March 8, 2020–April 19, 2020)]:* Air temperature T_{air} increases significantly and mostly stays above melting point even with daily fluctuations of more than 10 °C. The snowpack starts to melt evidenced by continuously high WC_S and steadily decreasing h_S throughout P7. Decrease in SWE is delayed by approximately one month compared to the decrease in h_S as the result of snow compaction.

Of all the snow, subnivean ground layer, and meteorological SPs in Fig. 4, the effects of snow liquid water-column WC_S and, to a lesser extent, onset of snow cover represented by h_S on $\sigma^0_{VV}(f)$ are clear. These effects are explained with some distinguishable examples. During the dry snow periods P3 and P5, σ^0_{VV} takes on an almost steady trend; however, with fluctuating WC_S during early spring (P6) and snow melt (P7) periods, backscattering at all frequencies fluctuates in response to WC_S. Fig. 5(a)–(c) shows a zoomed-in view of $\sigma^0_{VV}(f)$, WC_S, and T_{air}, respectively, during snow melt period (P7). It is evident that all three parameters show a diurnal fluctuation. Fluctuations of WC_S are delayed by 2–5 h with respect to T_{air} due to ice latent heat and thermal insulation of snow [5]. It is noteworthy that the aforementioned delay has an inverse relation with the observation frequency. Nevertheless, WC_S from L-band radiometry provides a comprehensive insight to the temporal evolution of $\sigma^0_{VV}(f)$, influenced by varying snow liquid water content, without the WC_S retrievals reaching saturation.

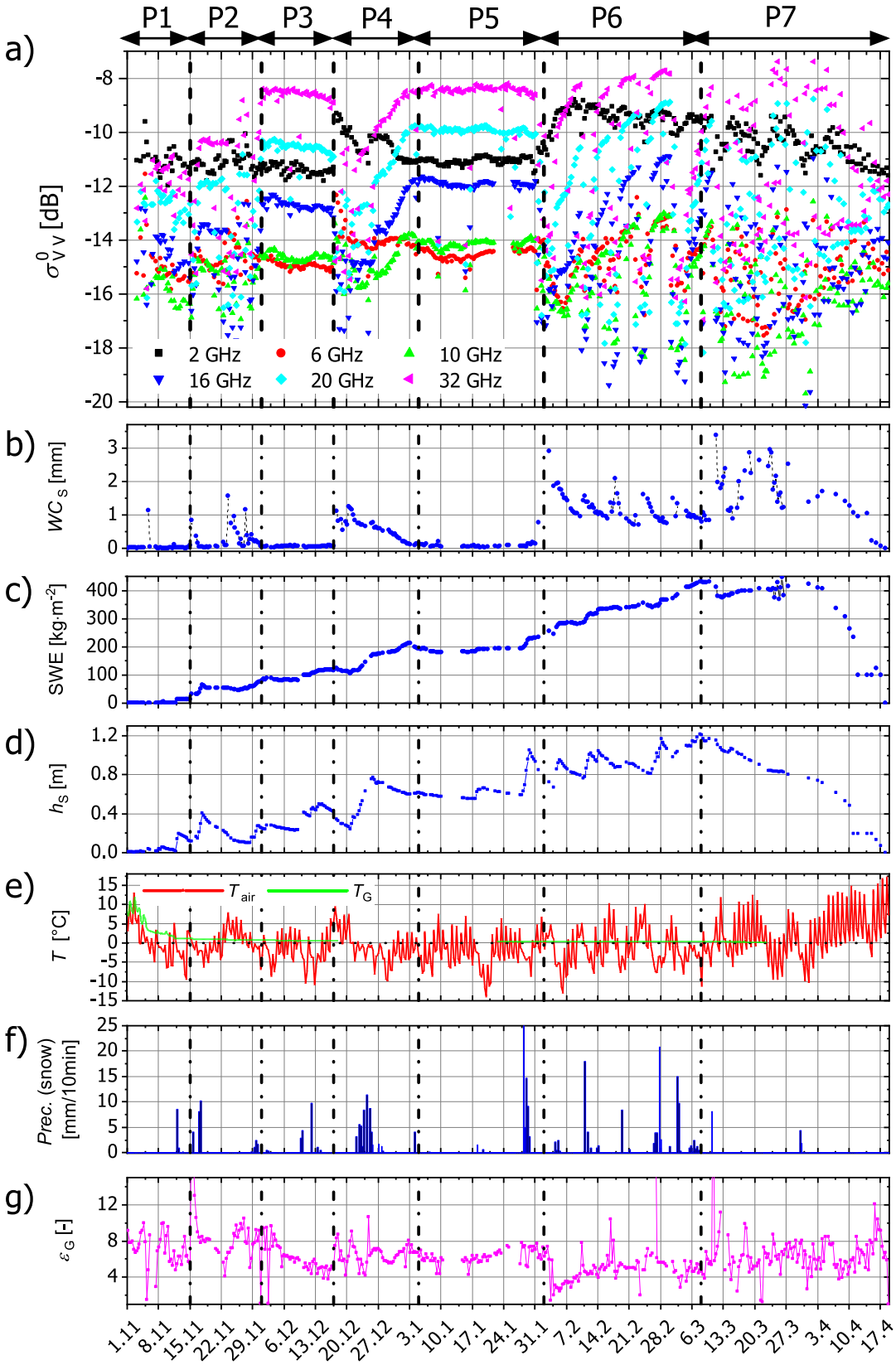

Fig. 4. Time series of (a) backscattering coefficeint $\sigma^0_{VV}(f)$ and (b) snow liquid water column WC_S retrieved from L-band radiometry. (c)–(g) *In situ* measured SWE, snow height h_S, ground and air temperature, snow precipitation, and ground permittivity, respectively.

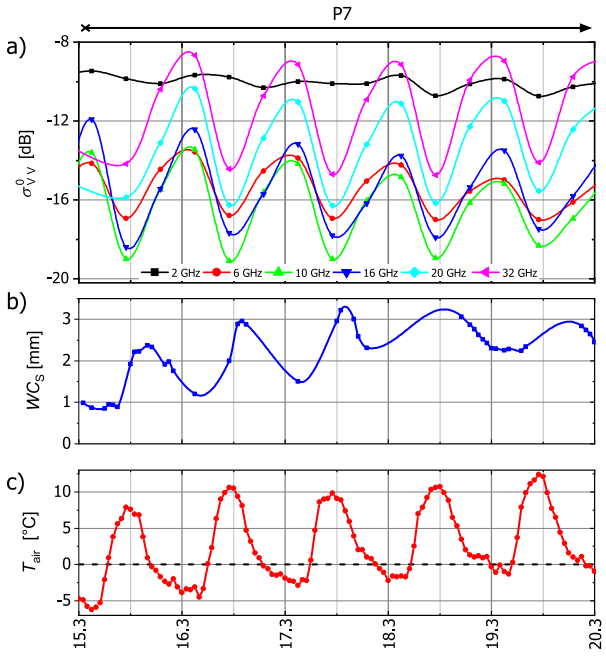

Fig. 5. Anticorrelated response of $\sigma^0_{VV}(f)$ to daily fluctuations of WC_S and T_{air} in snow melt period.

Increasing liquid water means higher propagation losses at all frequencies leading to decreasing $\sigma^0_{VV}(f)$ [39]. The frequency dependence of this effect is highlighted by pointing out the average fluctuation amplitude of $\sigma^0_{VV}(f)$, which is about 5.5 dB at $f = 32$ GHz and only ~0.8 dB at $f = 2$ GHz. It is noteworthy that, for dry snow, the penetration depth of microwaves is >100 m at 2 GHz [53] and decreases to about 1 m at 40 GHz [39]. This partially explains the qualitative assessment of the relative influence intensities (negligible, medium, and high) assigned to the different scattering elements (air–snow interface, snow volume, and snow–ground interface) for wet snow scenarios outlined in Table II (cases 2, 4, and 6). At high frequencies, with high propagation losses (low penetration depths) in the uppermost few millimeters to centimeters of the snowpack, the air–snow surface is the major scattering element, while, during the snow melt period (P7), the ground is almost entirely invisible to high-frequency microwaves (Ku–Ka bands). This finding is supported by previous works, such as [25] and [39]. Accordingly, the snow–ground interface has a negligible scattering contribution leaving a medium (to negligible) contribution from the snow volume, which itself depends on the actual liquid water content and height of the snowpack. Similarly, for "low" (1–4 GHz) and "intermediate" (4–12 GHz) frequency observations, during wet snow conditions, the snow–ground interface becomes a negligible scattering element (cases 2 and 4 in Table II).

Fig. 4 clearly shows an effect of snow liquid water column WC_S on backscatter $\sigma^0_{VV}(f)$, and Fig. 5 highlights this relationship and demonstrates the anticorrelation between WC_S and $\sigma^0_{VV}(f)$. To investigate this relationship, scatter plot of $\sigma^0_{VV}(f)$ versus WC_S are shown in Fig. 6(a)–(c), where the panel refer to the "low," "intermediate," and "high" FBs defined in Table II. Fig. 6(d)–(f) are prepared based on the data in Fig. 6(a)–(c) to highlight the key features of the data shown in the scatter plots. To this aim, the average $\sigma^0_{VV}(f)$ for given ranges of WC_S at each frequency is computed and plotted. The error bars indicate the standard deviation of each statistical sample. Here, we emphasize that this is not a polynomial fitting exercise, rather a more compact statistical representation of the same data in Fig. 6(a)–(c).

The following key observations are made based on the plots of $\sigma^0_{VV}(f)$ versus WC_S in Fig. 6:

1) According to Fig. 6(a)–(c), for nearly dry snow (0 mm $\leq$ WC$_S$ $\leq$ 0.25 mm), backscattering coefficient σ^0_{VV} at no frequency shows any relationship with snow liquid water column. This is expected from respective low penetration loss of microwaves in dry snow. This also implies the higher relevance of the snow–ground interface and snow volume as scattering elements. It also explains why the air–snow interface's relative scattering contribution at all bands is set to "negligible" for dry snow in Table II (cases (1), (3), and (5)).
2) For wet snow and at "low" and "intermediate" frequencies, there exists a clear anticorrelation between $\sigma^0_{VV}(f)$ and WC_S. Panels (d) and (e) in Fig. 6 demonstrate this inverse relationship, which results in ~4-dB drop in σ^0_{VV} in the range 1 mm $\leq$ WC$_S$ $\leq$ 2 mm for "low" frequencies (panel (d)) and ~2.2 dB drop in σ^0_{VV} in the range 0.6 mm $\leq$ WC$_S$ $\leq$ 1.7 mm for "intermediate" frequencies. Panels (d) and (e) in Fig. 6 show that the definition of snow wetness states depends on the frequency of observation. Accordingly, for "low" and "intermediate" frequencies, "wet" snow refers to $WC_S \geq 1$ mm and $WC_S \geq 0.6$ mm, respectively.
3) Scatter plots in Fig. 6(a)–(c) show that for high snow wetness $WC_S \geq (2\text{ mm}, 1.7\text{ mm}, 1\text{ mm})$ for "low," "intermediate," and "high" frequencies, respectively, the sensitivity of backscattering coefficient to snow liquid water column decreases, and thus, their anticorrelation diminishes. Only less than 5% of the total data lie at $WC_S \geq 2$ mm; therefore, extra caution must be used in drawing conclusions on the relationship between $\sigma^0_{VV}(f)$ and WC_S in this range [especially in Fig. 6(d) and (e)].
4) At "high" frequencies (see Fig. 6(c) and (f)), except for a generally decreasing $\sigma^0_{VV}(f)$ with increasing WC_S, no firm conclusion can be drawn on the relationship between $\sigma^0_{VV}(f)$ and WC_S. This is also clear from the generally larger error bars in Fig. 6(f) compared to the ones in Fig. 6(d) and (e) for every given WC_S. As reflected in Table II (case 6) for wet snow, the main scattering element is the air–snow interface where snow surface roughness plays a key role.
5) According to Fig. 6(a), $\sigma^0_{VV}(f)$ initially increases with increasing snow liquid water column 0.25 mm $\leq$ WC$_S$ $\leq$ 1 mm before taking on the inverse relationship described in Point 2 above. At this range of WC_S, the snowpack is still semitransparent at low frequencies, meaning that backscattering from snow–ground interface is noticeable. Simultaneously, liquid water enhances the snow volume scattering. This is because structural heterogeneities inside snow volume become more effective scatterers when their

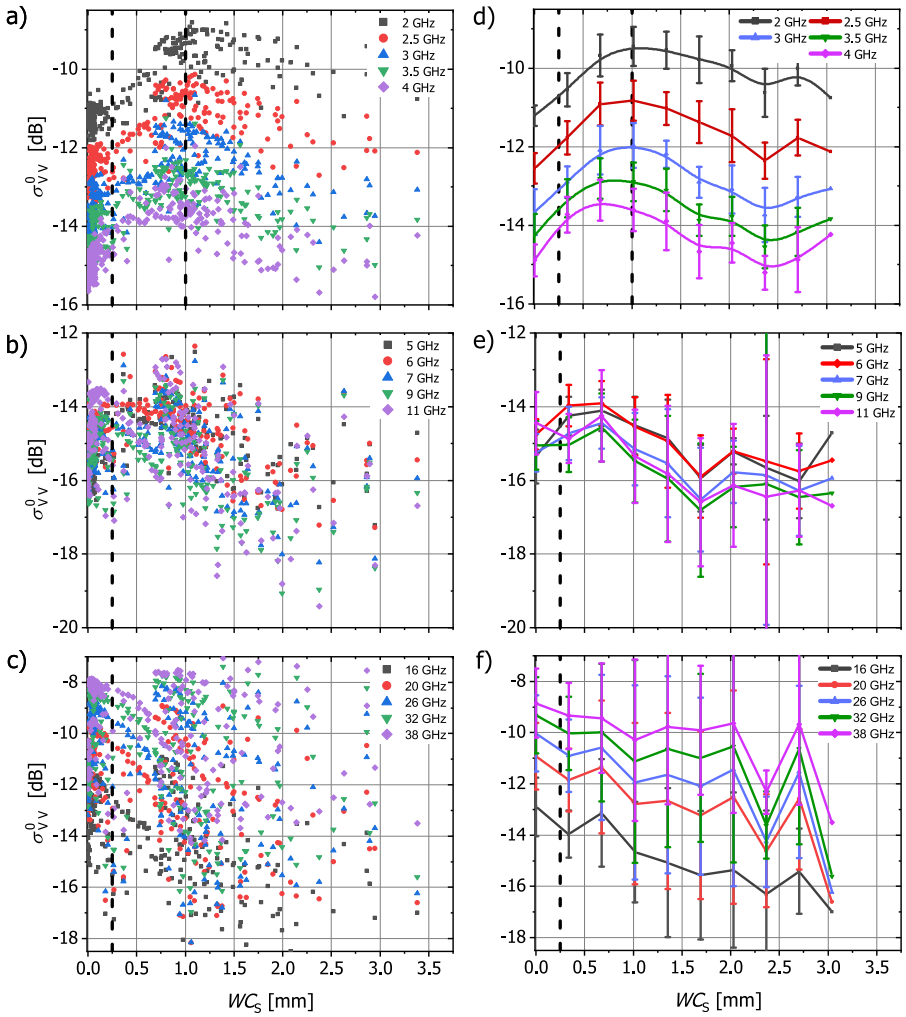

Fig. 6. Scatter plots of $\sigma^0_{VV}(f)$ versus WC_S for measurements conducted at (a) L- and S-bands, (b) C- and X-bands, and (c) Ku- to Ka-bands. (a)–(c) Scatter plots of individual date points. (d)–(f) Statistical mean and standard deviation of $\sigma^0_{VV}(f)$ for ten bins of 0 mm $\leq WC_S \leq$ 3 mm. Standard deviation is shown as vertical error bars at each data point.

permittivity increases with increasing snow liquid water content. These two mechanisms (backscatter from the ground and snow volume scattering) have a reinforcing effect resulting in higher $\sigma^0_{VV}(f)$. However, the losses for wet snow ($WC_S \geq 2$ mmm) create an opaque snowpack and, thus, negligible backscattering from the snow–ground interface (case (2) in Table II).

It is reiterated that WC_S on the horizontal axis of plots in Fig. 6 is estimated from L-band radiometry, which has a larger penetration depth in moist snow compared to measurements at higher frequencies. The lack of a clear correlation between WC_S retrieved from L-band radiometry and $\sigma^0_{VV}(f)$ measured at the highest FBs (see Fig. 6(c)) is expected. Accordingly, WC_S is much more representative of the snowpacks' liquid water-column, while $\sigma^0_{VV}(f)$ at 16–38 GHz is predominantly sensing liquid water in the snowpack's near surface layer.

As mentioned earlier in this section, in addition to WC_S, the backscattering coefficient shows a distinguishable response to the onset of snow cover represented by h_S. Fig. 7(a)–(c) shows the time series of $\sigma^0_{VV}(f)$, h_S, and T_{air} for the first month of snow cover over the site. P1, P2, and P3 refer to the snow-free period, first period of thin moist snow, and first period of dry snow, respectively. Fig. 7 shows that, with the snowpack reaching $h_S = 0.4$ m, $\sigma^0_{VV}(32$ GHz) increases, on average, by ~1.9 dB during the period November 6–20, 2019. With the start of P3 and due to effective dry snow volume scattering, $\sigma^0_{VV}(32$ GHz) reaches average values of ~ -8.5dB creating a relative difference of ~3.6 dB compared to the snow-free P1. This suggests that higher frequency measurements (such as 32 GHz) can be used for detection of the onset of snow especially if the snowpack is dry.

Between November 11 and 16, 2019, there exists only a thin snow cover ($h_S < 0.2$ m). Accordingly, on November 11, increasing T_{air} to ~ 5 °C causes snow melt and a drop of $\lesssim$2 dB in $\sigma^0_{VV}(32$ GHz) because: 1) due to the thin snowpack, volume scattering is negligible and 2) snow wetness causes high propagation loss. With T_{air} falling below 0 °C, $\sigma^0_{VV}(32$ GHz) rises by about 1 dB from the evening of November 11 until the morning of November 14. Once again with $T_{air} > 0$ °C from the afternoon of November 14 until late

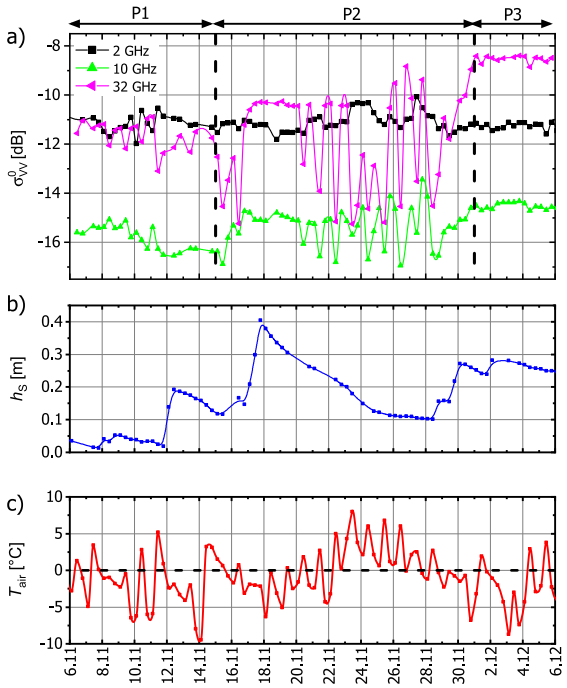

Fig. 7. Time-domain backscattering coefficient response to the onset of snow cover.

evening of November 15, σ^0_{VV}(32 GHz) drops by ~ 2.5 dB. The aforementioned issues together decrease σ^0_{VV}(32 GHz) compared to thicker and/or dry snowpack. The fluctuations of T_{air} between November 21 and 29, 2019, induce daily fluctuations of WC_S. Similarly, as discussed in Fig. 5, the amplitudes of daily $\sigma^0_{VV}(f)$ fluctuations seen in Fig. 7 increase with increasing measurement frequency.

It is highlighted here that the onset of snow cover has no prominent signature on σ^0_{VV}(6 GHz), and it is practically undetectable by σ^0_{VV}(2 GHz). However, a similar investigation of measurements at all available frequencies suggests that reliable detection of the onset of snow cover is possible using $\sigma^0_{VV}(f)$ at Ku- to Ka-bands.

B. Second-Order Response in Form of Cross-Correlation

In Section IV-A, the first-order response of $\sigma^0_{VV}(f)$ to snow liquid water column and the onset of snow cover was investigated. In that case, the sensitivity of measured $\sigma^0_{VV}(f)$ to the SPs WC_S and h_S is apparent directly from the respective time series (see Figs. 4, 5, and 7) or scatter plots (see Fig. 6). It is known that other SPs—such as precipitation and ground layer permittivity—influence the $\sigma^0_{VV}(f)$. However, their effects may not be recognizable from the respective time series or scatter plots. Therefore, we examine these relations by looking into time series of coefficients of determination $R^2(SP, \sigma^0_{VV}(f))$ between $\sigma^0_{VV}(f)$ and SPs $SP = (\epsilon_G, SWE, Prec.)$. This allows us to explore how each SP influences $\sigma^0_{VV}(f)$ over the course of the winter. The selected $SP = (\epsilon_G,\ SWE,\ Prec.)$ directly affect the scattering via the scattering elements given in Table II. The selected $(\epsilon_G,\ SWE,\ Prec.)$ have different characteristic time scales of temporal evolution. For example, in the presence of snow cover, ϵ_G is expected to change on a longer time scale than just a few hours [8], [14], whereas precipitation (*Prec.*) can change the snowpack conditions on the order of hours. Thus, the length of the asymmetric moving time window used for correlation computation should be chosen accordingly to best capture the time scale of each SP's impact on the backscatter $\sigma^0_{VV}(f)$. Too short of a time window would cause nonphysical correlation anomalies and suffer from low statistics at the available measurement rate of approximately eight hours. Conversely, too long of a time window would result in smearing out the SPs' impact on $\sigma^0_{VV}(f)$. We further emphasize that the coefficient of determination $R^2(SP, \sigma^0_{VV}(f))$ used in our study features peaks and dips that are delayed by the chosen length of the time window compared to associated responses in $\sigma^0_{VV}(f)$.

Fig. 8 shows the time series of $\sigma^0_{VV}(f)$ (a) and the coefficient of determination $R^2(\epsilon_G, \sigma^0_{VV}(f))$ (b) with respect to ground permittivity computed for a correlation time window of 14 days. The clearly higher $R^2(\epsilon_G, \sigma^0_{VV}(f))$ during dry snow periods P3 and P5 are indicative of a stronger influence of ϵ_G on $\sigma^0_{VV}(f)$ due to the semitransparency of dry snowpack especially at "low" and "intermediate" frequencies. Note that peaks and other features in $R^2(\epsilon_G, \sigma^0_{VV}(f))$ are shifted by 14 days as a result of the 14-day moving correlation time window. These two examples in Fig. 8(b) explain the assignment of "high" to snow–ground interface at "low" to "intermediate" FBs under dry snow conditions (cases (1) and (3) in Table II). Around January 25, 2020, $R^2(\epsilon_G, \sigma^0_{VV}(f))$ reaches a maximum whereby $R^2(\epsilon_G, \sigma^0_{VV}(f))$ increases with decreasing frequency such that, for L- to X-bands, $R^2(\epsilon_G, \sigma^0_{VV}(f)) \geq 0.4$. For Ku- to Ka-bands, the coefficient of determination is lower than 0.4 but with the same frequency dependence as "low" and "intermediate" FBs. This shows that, under dry snow conditions with $h_S \approx 0.7$ m, at higher microwave frequencies, most of the backscattering contribution originates from the snow volume (case (5) in Table II). However, this is not the case when the snowpack is dry and thin, making volume scattering an inefficient scattering mechanism. This reflects in loss of the frequency dependence of $R^2(\epsilon_G, \sigma^0_{VV}(f))$ during P3 peaking on December 19, 2019. At this time, increased coefficient of determination (compared to preceding and succeeding weeks) shows increased relevance of the snow–ground interface, while lack of frequency dependence implies less effective volume scattering.

At the beginning of early spring period (P6), the snow–ground interface still has a detectable influence on σ^0_{VV}(2 GHz), which is manifested by $R^2(\epsilon_G, \sigma^0_{VV}(2\text{ GHz})) \approx 0.1$ between February 25 and March 5, 2020. This is because snowpack, with 1 mm $\leq WC_S \leq$ 2 mm (see Fig. 4), is still partially transparent at the L-band ($f = 2$ GHz). However, $R^2(\epsilon_G, \sigma^0_{VV}(f))$ is negligible at all FBs during snow melt period (P7) due to complete opacity of wet snow.

In the next step, we study the coefficient of determination $R^2(SWE, \sigma^0_{VV}(f))$ between SWE and $\sigma^0_{VV}(f)$ with SWE considered as a major contributor to the "snow volume" scattering regime (see Table II). For a snowpack with uniform

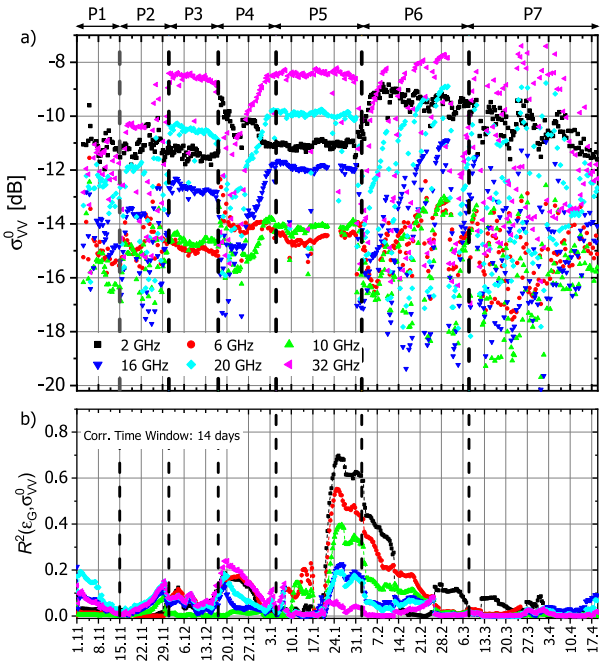

Fig. 8. Coefficient of determination $R^2(\epsilon_G, \sigma^0_{VV}(f))$ calculated based on a 14-day asymmetric moving window.

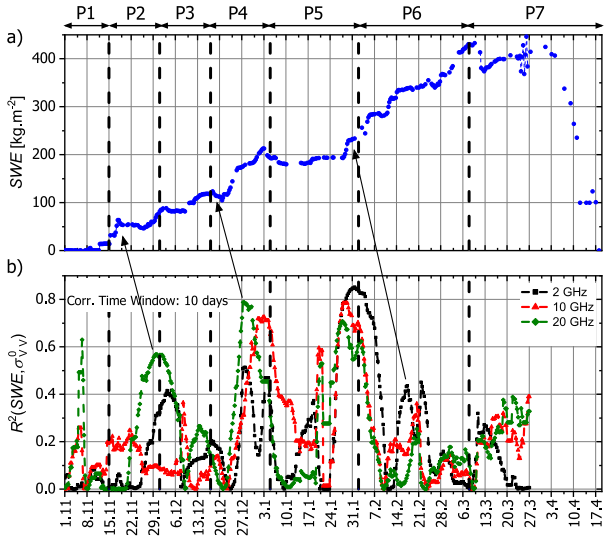

Fig. 9. (a) Time series of *in situ* measured SWE and (b) coefficient of determination $R^2(SWE, \sigma^0_{VV}(f))$ for $f = 2$, 10, and 20 GHz.

density profile, *SWE* is computed using $SWE = \rho_S \cdot h_S$. Therefore, generally, SWE changes with changing h_S (for example snowfall) and $\rho_S(z)$ (metamorphosis and densification due to gravity and melt).

Fig. 9(a) shows the time series of *in situ* measured SWE and Fig. 9(b) shows coefficient of determination $R^2(SWE, \sigma^0_{VV}(f))$ computed using a ten-day moving correlation time window. The ten-day window is selected based on the knowledge that the rate of change for *SWE* is expectedly faster than ϵ_G. In Fig. 9, only $R^2(SWE, \sigma^0_{VV}(f))$ for $f = 2$, 10, and 20 GHz is shown for better readability. Considering the ten-day delay of peaks and signal features in $R^2(SWE, \sigma^0_{VV}(f))$, it is observed that the effect of *SWE* on $\sigma^0_{VV}(f)$ is noticeable—$R^2(SWE, \sigma^0_{VV}(f)) \geq 0.4$—almost exclusively up until the end of the second dry snow period (P5). In other words, *SWE* has a distinguishable effect on $\sigma^0_{VV}(f)$ in all snowpack conditions other than thick wet snowpack. The first strong peak in $R^2(SWE, \sigma^0_{VV}(f))$ at $f = 2$ and 20 GHz takes place during P2 with thin moist snow, and the second and third strong peaks (∼December 30, 2019, and ∼January 27, 2020) take place during P3 and P5 (considering the ten-day shift) under dry snow conditions.

With the beginning of early spring period (P6) and appearance of high amounts of liquid water in snow, the relationship between SWE and backscattering coefficient is weakened due to increasing opacity of wet snow. Like the case of $R^2(\epsilon_G, \sigma^0_{VV}(2\text{ GHz}))$ in Fig. 8, SWE shows a noticeable degree of influence on $\sigma^0_{VV}(2\text{ GHz})$, with $R^2(\epsilon_G, \sigma^0_{VV}(2\text{ GHz})) \approx 0.43$ on February 17 and 21, 2020, due to lower penetration losses, which later vanishes with increasing WC_S.

Investigation of the coefficient of determination between *SWE* and $\sigma^0_{VV}(f)$ shows that, whenever $R^2(SWE, \sigma^0_{VV}(f))$ reaches a relatively high value of >0.4 during P2–P5, unlike $R^2(\epsilon_G, \sigma^0_{VV}(f))$ in Fig. 8, no direct or inverse frequency dependence can be observed for $R^2(SWE, \sigma^0_{VV}(f))$. This is indicative of two points.

1) Considering only SWE for representing the effect of snow volume scattering especially at higher frequencies may be too simplistic. Other parameters such as correlation length of snow microstructure, obtainable with, e.g., X-ray tomography [54] and snow evolution models, should be considered. However, X-ray tomography can only be used for field experiments but is not applicable in large-scale studies and operational data products.
2) Because, under certain snowpack conditions, $R^2(SWE, \sigma^0_{VV}(f))$ reaches a maximum at different frequencies, a successful SWE retrieval approach may require multifrequency $\sigma^0_{VV}(f)$.

It is key to note that, during P2–P5, $R^2(SWE, \sigma^0_{VV}(f))$ seems to increase in response to changes in *SWE*, and whenever SWE takes on a steady trend with $\delta SWE/\delta t \approx 0$ kg·m^{-2}·s^{-1}, $R^2(SWE, \sigma^0_{VV}(f))$ is minimized. We emphasize that small changes in the selected length of the time window (± one or two days) does not significantly change the presented result.

Snow precipitation (*Prec.*) is the last SP whose influence on the backscattering coefficient is studied in Fig. 10. Alpine precipitation events often take place on time scales of less than an hour up to a day. Precipitation changes snow surface and volume properties, including snow height, surface wetness and permittivity, density, and surface roughness. Therefore, the effects of precipitation on states of the snow–ground system can remain longer than the actual duration of an individual precipitation event. Fig. 10(a) shows the time series of precipitation, and Fig. 10(b) shows the coefficient of determination $R^2(Prec., \sigma^0_{VV}(f))$ computed using an asymmetric two-day moving window. The two-day window is selected to be as short as possible to capture the short-term influence of precipitation on the measured backscattering coefficient

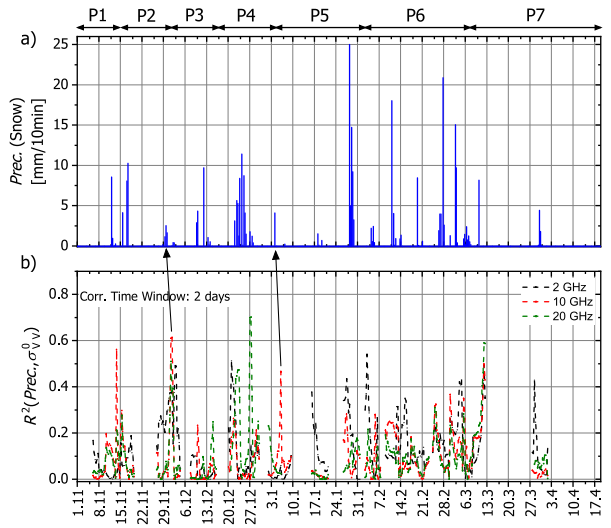

Fig. 10. (a) Snow precipitation and (b) coefficient of determination $R^2(Prec., \sigma^0_{VV}(f))$ for $f = 2$, 10, and 20 GHz.

and still provide acceptable statistics considering the available measurement interval of approximately 8 h. Like Fig. 9(b), coefficient of determination is shown only for $f = 2$, 10, and 20 GHz for better readability.

Fig. 10(b) shows a clear response from backscattering coefficient to snow precipitation events such that $R^2(Prec., \sigma^0_{VV}(f))$ increases to a maximum, with a delay of less than a day, before decreasing again and, in many cases, resting at 0. An example is the precipitation between November 29 and 30, 2019, where $R^2(Prec., \sigma^0_{VV}(f))$ increases from < 0.1 and reaches its maximum $R^2(Prec., \sigma^0_{VV}(f)) \geq 0.5$ on December 1, 2019, and then decreases to 0 on December 2, 2019. A similar pattern exists for every precipitation event; however, it can happen that the response to precipitation in form of increased $R^2(Prec., \sigma^0_{VV}(f))$ is not present at all frequencies. For example, the precipitation on January 4, 2020, sparks a response at $f = 10$ GHz with reaching a maximum $R^2(Prec., \sigma^0_{VV}(10\ \text{GHz})) \approx 0.5$ on January 6, 2020, whereas the other two frequency measurements lack a clear response. Specific reasons to why $\sigma^0_{VV}(f)$ in a certain frequency range responds or not to a precipitation event requires case-by-case simulation and analysis of the backscatter expected from the snow–ground compartment in a specific state. However, SPs, such as wetness of precipitated snow, air temperature, snowpack wetness, and surface roughness, are among some of the main causes of frequency-specific responses to precipitation.

The key takeaway message from Fig. 10 is the short-term (compared to other examined SPs with second-order effects) response of $\sigma^0_{VV}(f)$ to precipitation, which is detectable at all or some of the FBs.

The analyses and findings presented in Sections IV-A and IV-B on the first- and second-order responses of backscattering coefficient to the investigated SPs are also valid for $\sigma^0_{VV}(f)$ measured at other nadir angles $\theta = 25°$ and 45°. Theoretical investigation of the effect of the nadir observation angle on such inter-relationships was performed previously in other works, such as [55], and their experimental validation is outside the scope of this article.

The analyses in this section show that, even when $\sigma^0_{VV}(f)$ is steady over periods P3 and P5 with no obvious connection to measured snow and ground SPs (see Fig. 4), these parameters continue to influence $\sigma^0_{VV}(f)$ at their own characteristic time scale. Our methodology looks into coefficients of determination $R^2(SP, \sigma^0_{VV}(f))$ between $\sigma^0_{VV}(f)$ and state parameters $SP = (\epsilon_G,\ SWE,\ Prec.)$ influencing the backscatter $\sigma^0_{VV}(f)$ of the ground–snow compartment at different time scales. This allows us to highlight the strength and frequency dependence of the system's response to a given SP's variations. For example, during P5, the backscattering coefficient does not show any sensitivity to WC_S and h_S, but it responds to ϵ_G, *SWE*, and precipitation, as discussed in Figs. 8–10, respectively. There are SPs other than $SP = (\epsilon_G,\ SWE,\ Prec.)$ that influence scattering elements defined in Table II. The SPs investigated in this section are those available from our measurements during campaign. Other influential SPs can be investigated in a similar fashion.

It is important to point out that the results in Section IV with respect to the first- and second-order responses of $\sigma^0_{VV}(f)$ to WC_S, onset of snow cover, SWE, and snow precipitation are also true for $\sigma^0_{VV}(f)$ measured over the "natural ground area" and not only the presented "charcoal–sand area." Due to a hardware failure, two approximately one-month gaps exist in *in situ* measured permittivity of natural ground. Therefore, we could not perform a similar analysis, as presented in Fig. 8 for "natural ground area."

V. Conclusion and Summary

The time series of calibrated backscattering coefficients and several key snow, ground, and meteorological SP measurements, conducted during the Winter 2019/2020 campaign at the Davos-Laret Remote Sensing Field Laboratory, were presented. The overarching research question in this article is the identification of the relative strength of the primary scattering elements in the snow–ground system and their contribution to copol $\sigma^0_{pp}(f)$. Accordingly, three main scattering elements were defined: 1) air–snow interface; 2) snow volume; and 3) snow–ground interface. Numerous snow and subnivean ground SPs simultaneously and nonlinearly influence backscatter. To address our research question, we introduced Table II, based on the understanding that observation frequency (f) and snow liquid water content are the two most prominent parameters affecting $\sigma^0_{pp}(f)$. This table presented the strength of a defined scattering element (surface and volume) "relative" to other elements.

It was shown that backscatter from snow has an inverse relationship with snow liquid water column under wet snow conditions. This relationship was experimentally demonstrated using the time series of $\sigma^0_{pp}(f)$ against T_{air} and WC_S and scatter plots of $\sigma^0_{pp}(f)$ versus WC_S. The latter highlights that this anticorrelation is stronger for higher frequencies due to frequency-dependent propagation losses by WC_S. In addition, it was shown that, at "low" frequencies and under moist snow conditions, $\sigma^0_{pp}(f)$ increases with increasing moisture content (until opaque). We hypothesized that a slight amount of liquid water within the snowpack can turn heterogeneities

of scattering structures within the snow volume more effective. This, together with scattering from the snow–ground interface, enhances the total backscattering. However, for wet snow conditions, the propagation losses limit the microwave penetration depth and, thus, lower the backscatter. This study makes synergistic use of passive and active microwave remote sensing. This is achieved by estimating WC_S from L-band radiometry and using it to study the effect of snow wetness on σ^0_{VV}.

It was demonstrated that the onset of snow cover can be detected using "high" frequency observations by the increase in $\sigma^0_{pp}(f)$. This detection method works for both new wet- and dry-thin (< 0.4 m) snow covers. However, the dry snow creates a much larger difference in $\sigma^0_{pp}(f)$ due to its more effective volume scattering.

We showed that the effects of several other SPs, such as $SP = (\epsilon_G, SWE, Prec.)$, can only be demonstrated with temporal analysis of the correlation between $\sigma^0_{pp}(f)$ and the SPs in terms of their coefficient of determination $R^2(SP, \sigma^0_{VV}(f))$. Results show that the snow–ground interface, and thus the ground permittivity, becomes an important scattering element under dry snow conditions. This influence is inversely related to the observation frequency. Furthermore, for any seasonal snowpack condition other than thick wet snowpack, $\sigma^0_{VV}(f)$ responds to SWE changes. This is manifested by increasing $R^2(SWE, \sigma^0_{VV}(f))$ in response to SWE variations. When investigating the effect of SWE on backscatter, emphasis is conventionally placed more on the phase decorrelation time. Here, we have shown that the time series of measured backscattering coefficient also contains extractable information about SWE. Furthermore, it was shown that the backscattering coefficient responds to snow precipitation but in a shorter time such that $R^2(Prec., \sigma^0_{VV}(f))$ increases with snowfall and later falls back to ~ 0 when such effects are overtaken by other more dominant scattering regimes.

To summarize, each SP affects $\sigma^0_{VV}(f)$ at their own intrinsic time scale, and their effect is heavily dependent on the snowpack wetness and the observation frequency. For example, during the dry snow periods, snow–ground interface becomes a more effective scattering element at "low" and "intermediate" frequencies; however, the time scale of such influence is in the order of weeks because snow–ground interface features (e.g., ϵ_G) change slowly in the presence of a thermally insulating snowpack. On the other hand, snowfall changes the snowpack conditions (e.g., h_S and SWE) in a few hours.

Table II can be considered a qualitative identifier of the main scattering elements under different snow conditions. This key knowledge can be used as a guide in any physics- or artificial-intelligence-based algorithm for the retrieval of snow SPs, such as SWE. Given the complexities of the interrelationship between $\sigma^0_{VV}(f)$ and measured SPs, we have shown that a successful universal approach for the retrieval of key snow properties will benefit from a broad range of multifrequency observations.

Another novel approach in this article is the use of L-band radiometry for the detection of snow wetness state as a key parameter in defining the strength of scattering regimes in the snow–ground system. This approach was shown to work in various regions of the cryosphere [3]–[5], [56] and affords the possibility of using the passive Soil Moisture and Ocean Salinity (SMOS) and SMAP satellite measurements in support of SWE retrieval using other active satellite measurements.

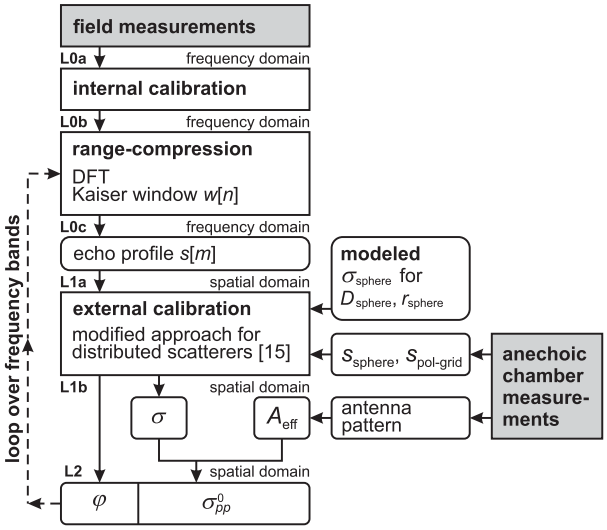

Fig. 11. Flowchart illustrating the WBSCAT data processing steps and intermediate data outputs.

The findings reported in this article are based on measurements conducted approximately every 8 h. It is vital to improve this temporal resolution of measurements to investigate more rapid changes in the snowpack, such as heavy snowfall and rain on snow, and their impact on $\sigma^0_{VV}(f)$. Additional measurements at finer temporal resolution are also expected to improve the reliability of this analysis and reveal further details. WBSCAT is a phase-coherent instrument and provides information on the signal phase. Therefore, future works should also the relationship between phase decorrelation time and snow–ground SPs.

Considering the characteristically different microwave penetration depths at the wide frequency range of L- to Ka-bands, we recommend performing wideband radiometry in future campaigns with an active/passive observation concept. This is because, while signal saturation at higher frequencies (e.g., Ku- to Ka-bands) is imminent with the appearance of melt water, the snow wetness flag provided by radiometry at these frequencies could prove useful for backscattering analysis.

Finally, it is prudent to: 1) apply the findings of this work in a retrieval algorithm with machine learning while maintaining a grasp on the ongoing physical processes and 2) assess the performance of such algorithms considering the available satellite remote sensing data in terms of frequency, spatial resolution, and revisit time.

APPENDIX
DATE PROCESSING METHOD TO ACHIEVE CALIBRATED σ^0_{pp}

This appendix is a concise explanation of the WBSCAT data processing method. The reader is referred to previous works [45], [47], [57], [58] for more detail information. The flowchart in Fig. 11 is a guiding illustration of different stages of the WBSCAT data processing explained subsequently.

TABLE III

FREQUENCY SUBBANDS AND PROCESSING PARAMETERS. KAISER WINDOW β IS SET TO 5 FOR QR800 AND 4 FOR THE OTHER TWO TYPES OF ANTENNAS

Antenna	f_{sub} [GHz]	B_{sub} [GHz]	δr [cm]
QR800	2, 2.5, 3, 3.5, 4, 4.5, 5	2.0	3.701
QR2000	4.5, 5, 6, 7, 8, 9, 10, 11, 12, 13, 14, 15, 16, 16.5	3.0	2.467
QR18000	18, 20, 22, 24, 26, 28, 30, 32, 34, 36, 38	4.0	2.467

In this figure, different data outputs are indicated as "Levels" (L) and referred to where they are first defined and used in the text. Rectangles and squircles show "processes" and main intermediate output data, respectively. We categorized the data into L1, L2, and L3 related to the frequency domain, the spatial domain, and the backscattering coefficient.

WBSCAT measures microwave backscatter coefficients σ^0_{pp} at transmit/receive (TX/RX) polarization combinations $pp =$ HH, VV, and HV over the frequency range of 1–40 GHz. Accordingly, WBSCAT operates in three overlapping FBs: 1–6, 3–18, and 16–40 GHz. Unambiguous maximum range distance was chosen as $R_{\max} = 60$ m for the lowest FB and $R_{\max} = 30$ m for the two higher FBs [46], [58]. For each FB, a pair of identical quad-ridged (QR) horn antennas [59] is used. These dual-polarization antennas are constructed to have nearly identical radiation patterns for H- and V-polarizations. More details on these antennas are given at the end of this appendix and in Fig. 12.

Radiometric calibration of the backscatter data is performed in three steps over the backscatter data [58]:

1) The VNA is calibrated using the short, open, load, through (SOLT) calibration standards. The calibrated VNA is then used to measure the S-parameters of the RA and TA low-noise amplifiers (LNAs), including the associated system elements, such as attenuators and cables. The measured data (L0a in Fig. 11) are corrected for the contributions of switches, LNAs, and attenuators within the Microwave Assembly (L0b) using network deembedding [60] and then range-compressed (L1a) as previously described.
2) The range echo profiles $s[m]$ are then corrected for antenna cables and connectors that are outside of the internal calibration loop using the same deembedding method. The characteristics of these elements are considered stable and were measured prior to assembly of WBSCAT. It is noteworthy that range compression is performed to transform the L0a WBSCAT measured scattering parameters (for each frequency and combination of transmitted and received polarization) into a range echo profile $\tilde{s}[m]$. Table III shows the subband center frequencies f_{sub} and bandwidths, as well as the range sample spacing δr for three FBs operated with three pairs of QR horn antennas.
3) The backscatter data are corrected for antenna propagation loss and antenna gain to obtain the calibrated RCS σ. This step of the calibration is based on the method proposed in [61]. This method requires backscattering measurements of the copol (sphere) and cross-pol (polarization grid) calibration targets together with their modeled radar cross section. As illustrated in Fig. 11, the measurements on calibration targets were performed in an anechoic chamber and fed into the processing chain.

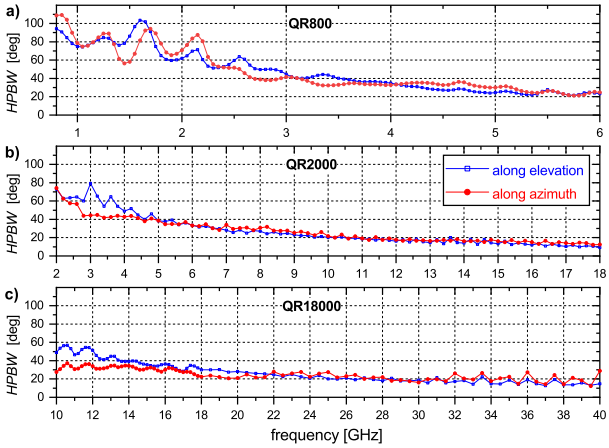

Fig. 12. Half-power beamwidth of the QR horn antennas used in WBSCAT for its three FBs ranging from 1 to 40 GHz.

Calculation of the normalized RCS (i.e., backscattering coefficient σ^0), given the calibrated RCS, $\sigma = |\tilde{s}^u_{pp}|^2 \cdot 4\pi$, requires knowing the effective area of the illuminated surface A_{eff}. The effective illuminated area A_{eff} at each ground range ρ is obtained by integration of the surface area weighted by the two-way antenna pattern normalized to peak gain [58]. A_{eff} is calculated for all combinations of receive and transmit polarizations and each slant range r_{u}. Accordingly, the backscattering coefficient at a specific incidence angle θ is computed as

$$\sigma^0 = \sigma / A_{\text{eff}}. \tag{1}$$

Half-Power Beamwidth of the Quad-Ridged Horn Antennas:

Fig. 12 shows the HPBW of the QR800, QR2000, and QR2000 antennas provided by the manufacturer. The red and blue lines in each panel essentially indicate the HPBW for each of the two orthogonal ports of the antenna. These horn antennas, when operated in their designed frequency range, are more directive at higher frequencies. The QR antennas are designed for producing nearly identical radiation patterns along both H- and E-planes. However, a noticeable level of asymmetry still exists at the lower end of each antenna's designated frequency range. However, the asymmetry decays at higher frequencies. It should be noted that more important than symmetry is the quantitative knowledge of HPBW (in Fig. 12), for example, for the computation of the number of azimuth looks N_{az}. It is noteworthy that the isolation between the horizontal and vertical antenna ports is >33 dB for all three QR antenna pairs used in WBSCAT.

ACKNOWLEDGMENT

The European Space Agency provided the wideband scatterometer (WBSCAT). The authors would like to thank Henning Löwe and Matthias Jaggi at the WSL Institute for Snow and Avalanche Research (SLF, Davos) for conducting *in situ* weekly snow characterization.

REFERENCES

[1] W. Abdalati and K. Steffen, "Passive microwave-derived snow melt regions on the Greenland ice sheet," *Geophys. Res. Lett.*, vol. 22, no. 7, pp. 787–790, Apr. 1995.

[2] W. Abdalati and K. Steffen, "Snowmelt on the Greenland ice sheet as derived from passive microwave satellite data," *J. Climate*, vol. 10, no. 2, pp. 165–175, 1997.

[3] D. Houtz, R. Naderpour, M. Schwank, and K. Steffen, "Snow wetness and density retrieved from L-band satellite radiometer observations over a site in the west Greenland ablation zone," *Remote Sens. Environ.*, vol. 235, Dec. 2019, Art. no. 111361.

[4] R. Naderpour, D. Houtz, and M. Schwank, "Snow wetness retrieved from close-range L-band radiometry in the western Greenland ablation zone," *J. Glaciol.*, vol. 67, no. 261, pp. 27–38, 2021.

[5] R. Naderpour and M. Schwank, "Snow wetness retrieved from L-band radiometry," *Remote Sens.*, vol. 10, no. 3, p. 359, 2018.

[6] C. Sun, C. M. U. Neale, and J. J. Mcdonnell, "Snow wetness estimates of vegetated terrain from satellite passive microwave data," *Hydrol. Processes*, vol. 10, no. 12, pp. 1619–1628, Dec. 1996.

[7] A. E. Walker and B. E. Goodison, "Discrimination of a wet snow cover using passive microwave satellite data," *Ann. Glaciol.*, no. 17, pp. 307–311, 1993.

[8] J. Lemmetyinen *et al.*, "Snow density and ground permittivity retrieved from L-band radiometry: Application to experimental data," *Remote Sens. Environ.*, vol. 180, pp. 377–391, Jul. 2016.

[9] R. Naderpour, M. Schwank, C. Matzler, J. Lemmetyinen, and K. Steffen, "Snow density and ground permittivity retrieved from L-band radiometry: A retrieval sensitivity analysis," *IEEE J. Sel. Topics Appl. Earth Observ. Remote Sens.*, vol. 10, no. 7, pp. 3148–3161, Jul. 2017.

[10] M. Schwank *et al.*, "Snow density and ground permittivity retrieved from L-band radiometry: A synthetic analysis," *IEEE J. Sel. Topics Appl. Earth Observ. Remote Sens.*, vol. 8, no. 8, pp. 3833–3845, Aug. 2015.

[11] T. Zhao, L. Zhang, L. Jiang, S. Zhao, L. Chai, and R. Jin, "A new soil freeze/thaw discriminant algorithm using AMSR-E passive microwave imagery," *Hydrol. Processes*, vol. 25, no. 11, pp. 1704–1716, 2011.

[12] Y. Kim, J. S. Kimball, K. C. McDonald, and J. Glassy, "Developing a global data record of daily landscape freeze/thaw status using satellite passive microwave remote sensing," *IEEE Trans. Geosci. Remote Sens.*, vol. 49, no. 3, pp. 949–960, Mar. 2011.

[13] K. Rautiainen *et al.*, "Detection of soil freezing from L-band passive microwave observations," *Remote Sens. Environ.*, vol. 147, pp. 206–218, May 2014.

[14] M. Schwank and R. Naderpour, "Snow density and ground permittivity retrieved from L-band radiometry: Melting effects," *Remote Sens.*, vol. 10, no. 3, p. 354, Feb. 2018.

[15] C. Mätzler and E. Schanda, "Snow mapping with active microwave sensors," *Int. J. Remote Sens.*, vol. 5, no. 2, pp. 409–422, Mar. 1984.

[16] S. V. Nghiem and W.-Y. Tsai, "Global snow cover monitoring with spaceborne K_u-band scatterometer," *IEEE Trans. Geosci. Remote Sens.*, vol. 39, no. 10, pp. 2118–2134, Oct. 2001.

[17] L. Valenti, D. Small, and E. Meier, "Snow cover monitoring using multitemporal ENVISAT/ASAR data," in *Proc. 5th EARSeL Workshop, Remote Sens. Land Ice Snow*. European Association of Remote Sensing Laboratories, Feb. 2008, pp. 1–8. Accessed: Sep. 24, 2021, doi: 10.5167/uzh-6433.

[18] J. Shi and J. Dozier, "Inferring snow wetness using C-band data from SIR-C's polarimetric synthetic aperture radar," *IEEE Trans. Geosci. Remote Sens.*, vol. 33, no. 4, pp. 905–914, Jul. 1995.

[19] M. Bernier, J.-P. Fortin, Y. Gauthier, R. Gauthier, R. Roy, and P. Vincent, "Determination of snow water equivalent using RADARSAT SAR data in eastern Canada," *Hydrol. Processes*, vol. 13, no. 18, pp. 3041–3051, Dec. 1999.

[20] V. Conde, G. Nico, P. Mateus, J. Catalão, A. Kontu, and M. Gritsevich, "On the estimation of temporal changes of snow water equivalent by spaceborne SAR interferometry: A new application for the Sentinel-1 mission," *J. Hydrol. Hydromech.*, vol. 67, no. 1, pp. 93–100, 2019.

[21] Y. Cui *et al.*, "Estimating snow water equivalent with backscattering at X and Ku band based on absorption loss," *Remote Sens.*, vol. 8, no. 6, p. 505, 2016.

[22] A. Patil, S. Mohanty, and G. Singh, "Snow depth and snow water equivalent retrieval using X-band PolInSAR data," *Remote Sens. Lett.*, vol. 11, no. 9, pp. 817–826, Sep. 2020.

[23] C. Mätzler, "Notes on microwave radiation from snow samples and emission of layered snowpacks," Inst. Appl. Phys., Univ. Bern, Bern, Switzerland, Res. Rep. 96-09, Feb. 2004.

[24] A. Wiesmann and C. Mätzler, "Microwave emission model of layered snowpacks," *Remote Sens. Environ.*, vol. 70, no. 3, pp. 307–316, 1999.

[25] M. Proksch *et al.*, "MEMLS3&a: Microwave emission model of layered snowpacks adapted to include backscattering," *Geosci. Model Develop.*, vol. 8, no. 8, pp. 2611–2626, Aug. 2015.

[26] S. Tan, W. Chang, L. Tsang, J. Lemmetyinen, and M. Proksch, "Modeling both active and passive microwave remote sensing of snow using dense media radiative transfer (DMRT) theory with multiple scattering and backscattering enhancement," *IEEE J. Sel. Topics Appl. Earth Observ. Remote Sens.*, vol. 8, no. 9, pp. 4418–4430, Sep. 2015.

[27] S. Leinss, J. Lemmetyinen, A. Wiesmann, and I. Hajnsek, "Interferometric and polarimetric methods to determine SWE, fresh snow depth and the anisotropy of dry snow," in *Proc. IEEE Int. Geosci. Remote Sens. Symp. (IGARSS)*, Jul. 2015, pp. 1032–4029.

[28] J. Shi and J. Dozier, "Estimation of snow water equivalence using SIR-C/X-SAR. I. Inferring snow density and subsurface properties," *IEEE Trans. Geosci. Remote Sens.*, vol. 38, no. 6, pp. 2465–2474, Nov. 2000.

[29] R. Kwok *et al.*, "Intercomparison of snow depth retrievals over Arctic sea ice from radar data acquired by operation IceBridge," *Cryosphere*, vol. 11, no. 6, pp. 2571–2593, Nov. 2017.

[30] H. Lievens *et al.*, "Snow depth variability in the Northern Hemisphere mountains observed from space," *Nature Commun.*, vol. 10, no. 1, pp. 1–12, 2019.

[31] J. Shi and J. Dozier, "Estimation of snow water equivalence using SIR-C/X-SAR. II. Inferring snow depth and particle size," *IEEE Trans. Geosci. Remote Sens.*, vol. 38, no. 6, pp. 2475–2488, Nov. 2000.

[32] S. S. Board *et al.*, *Earth Science and Applications From Space: National Imperatives for the Next Decade and Beyond*. Washington, DC, USA: National Academies Press, 2007.

[33] J. Lemmetyinen *et al.*, "Nordic snow radar experiment," *Geosci. Instrum. Methods Data Syst.*, vol. 5, no. 2, pp. 403–415, 2016.

[34] J. Lemmetyinen *et al.*, "Analysis of active and passive microwave observations from the NoSREx campaign," in *Proc. IEEE Int. Geosci. Remote Sens. Symp.*, Jul. 2011, pp. 2737–2740.

[35] H. Rott *et al.*, "Cold regions hydrology high-resolution observatory for snow and cold land processes," *Proc. IEEE*, vol. 98, no. 5, pp. 752–765, May 2010.

[36] C. Derksen *et al.*, "Retrieving landscape freeze/thaw state from soil moisture active passive (SMAP) radar and radiometer measurements," *Remote Sens. Environ.*, vol. 194, pp. 48–62, Jun. 2017.

[37] J. Lemmetyinen *et al.*, "Retrieval of snow parameters from L-band observations—Application for SMOS and SMAP," in *Proc. IEEE Int. Geosci. Remote Sens. Symp. (IGARSS)*, Jul. 2016, pp. 7067–7070.

[38] J. R. Kendra, K. Sarabandi, and F. T. Ulaby, "Radar measurements of snow: Experiment and analysis," *IEEE Trans. Geosci. Remote Sens.*, vol. 36, no. 3, pp. 864–879, May 1998.

[39] H. Rott and C. Mätzler, "Possibilities and limits of synthetic aperture radar for snow and glacier surveying," *Ann. Glaciol.*, vol. 9, pp. 195–199, Jan. 1987.

[40] W. H. Stiles and F. T. Ulaby, "The active and passive microwave response to snow parameters: 1. Wetness," *J. Geophys. Res., Oceans*, vol. 85, no. C2, pp. 1037–1044, 1980.

[41] F. T. Ulaby, W. H. Stiles, L. F. Dellwig, and B. C. Hanson, "Experiments on the radar backscatter of snow," *IEEE Trans. Geosci. Electron.*, vol. 15, no. 4, pp. 185–189, Oct. 1977.

[42] F. T. Ulaby and W. H. Stiles, "The active and passive microwave response to snow parameters: 2. Water equivalent of dry snow," *J. Geophys. Res., Oceans*, vol. 85, no. C2, pp. 1045–1049, 1980.

[43] R. Naderpour, M. Schwank, and C. Mätzler, "Davos–Laret remote sensing field laboratory: 2016/2017 winter season L-band measurements data-processing and analysis," *Remote Sens.*, vol. 9, no. 11, p. 1185, Nov. 2017.

[44] M. Dimitrov *et al.*, "New improved algorithm for sky calibration of L-band radiometers JÜLBARA and ELBARA II," in *Proc. 12th Spec. Meeting Microw. Radiometry Remote Sens. Environ. (MicroRad)*, Mar. 2012, pp. 1–4.

[45] C. L. Werner *et al.*, "Processing and calibration of continuous snowpack measurements using the WBSCAT polarimetric microwave scatterometer during winter 2018–2019 at Davos Switzerland," in *Proc. AGU Fall Meeting*, 2019.

[46] C. Werner, M. Suess, U. Wegmüller, O. Frey, and A. Wiesmann, "The ESA wideband microwave scatterometer (WBSCAT): Design and implementation," in *Proc. IEEE Int. Geosci. Remote Sens. Symp. (IGARSS)*, Jul. 2019, pp. 8339–8342.

[47] C. Werner, O. Frey, U. Wegmüller, A. Wiesmann, and M. Suess, "The WBSCAT polarimetric synthetic aperture scatterometer for retrieval of *in-situ* time-series of snow structure," in *Proc. AGU Fall Meeting*, 2018.

[48] C. Mätzler, H. Aebischer, and E. Schanda, "Microwave dielectric properties of surface snow," *IEEE J. Ocean. Eng.*, vol. OE-9, no. 5, pp. 366–371, Dec. 1984.
[49] *Davos Laret (LAR) Primary CryoNet Station Information*. Accessed: Jun. 28, 2021. [Online]. Available: http://globalcryospherewatch.org/cryonet/sitepage.php?surveyid=194
[50] H. R. Bogena, J. A. Huisman, C. Oberdörster, and H. Vereecken, "Evaluation of a low-cost soil water content sensor for wireless network applications," *J. Hydrol.*, vol. 344, nos. 1–2, pp. 32–42, Sep. 2007.
[51] H. Bogena, J. Huisman, B. Schilling, A. Weuthen, and H. Vereecken, "Effective calibration of low-cost soil water content sensors," *Sensors*, vol. 17, no. 12, p. 208, Jan. 2017.
[52] T. Meissner and F. J. Wentz, "The complex dielectric constant of pure and sea water from microwave satellite observations," *IEEE Trans. Geosci. Remote Sens.*, vol. 42, no. 9, pp. 1836–1849, Sep. 2004.
[53] C. Mätzler, "Applications of SMOS over terrestrial ice and snow," in *Proc. 3rd SMOS Workshop*. Oberpfaffenhofen, Germany: DLR, 2001, pp. 10–12.
[54] F. Flin *et al.*, "Adaptive estimation of normals and surface area for discrete 3-D objects: Application to snow binary data from X-ray tomography," *IEEE Trans. Image Process.*, vol. 14, no. 5, pp. 585–596, May 2005.
[55] T. Strozzi and C. Matzler, "Backscattering measurements of Alpine snowcovers at 5.3 and 35 GHz," *IEEE Trans. Geosci. Remote Sens.*, vol. 36, no. 3, pp. 838–848, May 1998.
[56] D. Houtz, R. Naderpour, and M. Schwank, "Retrievals of snow properties over Greenland from L-band radiometry," in *Proc. IEEE Int. Geosci. Remote Sens. Symp. (IGARSS)*, Jul. 2019, pp. 3990–3993.
[57] A. Wiesmann *et al.*, "ESA SnowLab project: 4 years of wide band scatterometer measurements of seasonal snow," in *Proc. IEEE Int. Geosci. Remote Sens. Symp. (IGARSS)*, Jul. 2019, pp. 5745–5748.
[58] C. Werner, O. Frey, R. Naderpour, A. Wiesmann, M. Süss, and U. Wegmüller, "Aperture synthesis and calibration of the WBSCAT ground-based scatterometer," in *Proc. IEEE Int. Geosci. Remote Sens. Symp. (IGARSS)*, Jul. 2021, pp. 1947–1949.
[59] R. Dehdasht-Heydari, H. R. Hassani, and A. R. Mallahzadeh, "Quad ridged horn antenna for UWB applications," *Prog. Electromagn. Res.*, vol. 79, pp. 23–38, 2008.
[60] D. Agilent, "De-embedding and embedding s-parameter networks using a vector network analyzer," Agilent Technol., Santa Clara, CA, USA, Appl. Note 1364-1, May 2004, pp. 1–123.
[61] K. Sarabandi, F. T. Ulaby, and M. A. Tassouji, "Calibration of polarimetric radar systems with good polarization isolation," *IEEE Trans. Geosci. Remote Sens.*, vol. 28, no. 1, pp. 70–75, Jan. 1990.

Reza Naderpour received the M.Sc. degree in radio science and engineering from Aalto University, Espoo, Finland, in 2014, and the D.Sc. degree in environmental systems science from ETH Zürich, Zürich, Switzerland, in 2019.

During his time at Aalto University, he conducted research on a wide range of topics including radio wave propagation and channel modeling for 5G network research and development and space weather. He has participated in two scientific expeditions over the Greenland ice sheet and in the MOSAiC expedition in the central Arctic Ocean. His main areas of research are microwave remote sensing of the cryosphere, monitoring glacial, and sea ice dynamics. He also works on developing low-cost field-capable microwave instruments for measuring the dielectric properties of natural media.

Dr. Naderpour received the Silver Medal of ETH Zürich for distinguished doctoral theses in 2020.

Mike Schwank was born in Zürich, Switzerland, in 1966. He received the bachelor's degree in electrical engineering and the Ph.D. degree in physics from ETH Zürich, Zürich, in 1989 and 1999, respectively.

He has part-time employments with Gamma Remote Sensing Research and Consulting Ltd., Gümligen, Switzerland, from 2007 to 2009 and since 2013, and the Swiss Federal Research Institute WSL, Birmensdorf, Switzerland. He is experienced with industrial research and development in the fields of micro-optics and telecommunications from 1999 to 2003. He is also experienced with leading Ph.D. students and the coordination of large research projects, such as Terrestrial Environmental Observatories (TERENO). His current research interest includes microwave remote sensing studies in support of Soil Moisture and Ocean Salinity (SMOS) and future satellite missions.

Derek Houtz was born in Washington, DC, USA, in 1989. He received the Ph.D. degree in aerospace engineering specializing in microwave remote sensing and radiometer calibration from the University of Colorado at Boulder, Boulder, CO, USA, in 2017.

He has been engaged in environmental monitoring for over a decade. He has been bringing strong skills in hardware and software development, microwave radiometry, and field research implementation. With research assistant and post-doctoral positions at the National Institute of Standards and Technology (NIST), Gaithersburg, MD, USA, he developed traceable radiometer calibration sources. In parallel, he worked as a Field Assistant and a Data Analyst for the Greenland Climate Network (GC-Net) for the Cooperative Institute for Research in Environmental Studies (CIRES), Boulder, from 2013 to 2018. Joining the Swiss Federal Institute for Forest, Snow, and Landscape Research (WSL), Birmensdorf, Switzerland, in 2018, he has contributed to active and passive microwave remote sensing research for algorithm development, field campaigns, and hardware. In 2020, he founded TerraRad Tech AG, Zürich, Switzerland. He built the first TerraRad Tech L-band radiometer prototypes in the lab at WSL and applied for a European patent in 2020 based on a highly efficient L-band antenna.

Charles Werner (Life Senior Member, IEEE) received the M.S. degree in electrical engineering and the Ph.D. degree in systems engineering from the University of Pennsylvania, Philadelphia, PA, USA, in 1982 and 1987, respectively.

His Ph.D. work involved tomographic 3-D microwave and acoustic imaging. From 1982 to 1999, he was employed at the Jet Propulsion Laboratory, Pasadena, CA, USA, in radar system engineering for the earth and planetary synthetic aperture radar (SAR) systems, including the Cassini Radar Instrument and Shuttle Topographic Mapping Radar (SRTM) Missions. While being a Visiting Researcher at the University of Zurich, Zürich, Switzerland, from 1993 to 1995, he developed an end-to-end interferometric radar processing system for airborne and spaceborne SAR. Together with Urs Wegmüller, they founded Gamma Remote Sensing AG, Gümligen, Switzerland, in 1995. He is currently involved in the development of gamma's radar application software for the calculation of interferometric deformation time series, terrain geocoding, and visualization. He is also active in the development, design, and production of microwave instrumentation including ground-based Ku-band real-aperture radars for near real-time deformation monitoring, microwave radiometers, wideband microwave scatterometers, and SARs.

Christian Mätzler received the M.Sc. degree in physics with a minor in mathematics and geography and the Ph.D. degree in physics with a minor in solar radio astronomy from the University of Bern, Bern, Switzerland, in 1970 and 1974, respectively. He got the Habilitation in applied physics in 1986 and the title of a Titular Professor in 1992.

After post-doctoral research at the NASA Goddard Space Flight Center, Greenbelt, MD, USA, and the Swiss Federal Institute of Technology (ETH), Zürich, Switzerland, he became a Research Group Leader for terrestrial and atmospheric radiometry and remote sensing at the Institute of Applied Physics, University of Bern, in 1978. His teaching included principles of remote sensing, imaging radiometry, radar meteorology, and radiative transfer. After retirement in July 2010, he started as a consultant for Gamma Remote Sensing, Gümligen, Switzerland. His studies have concentrated on microwave (1–100 GHz) signatures for active and passive remote sensing of the atmosphere, snow, ice, soil, and vegetation, as well as on the development of methods for dielectric and propagation measurements for such media. He is an Editor of a book on thermal microwave emission with applications for remote sensing. Furthermore, he has been interested in special ice forms, such as hair ice.